Automatic Stereology of Mean Nuclear Size of Neurons using an Active Contour Framework

Hady Ahmady Phoulady[a], Dmitry Goldgof[a], Lawrence O. Hall[a], Kevin Nash[b], Peter R. Mouton[a,b,c]

[a]*Department of Computer Science and Engineering, University of South Florida, Tampa, FL*
[b]*Byrd Alzheimer's Disease Center and Research Institute, University of South Florida School of Medicine, Tampa, FL*
[c]*Department of Pathology & Cell Biology, University of South Florida School of Medicine, Tampa, FL*

Abstract

Quantification of stereological parameters such as area and volume on stained tissue sections is useful for a wide variety of biological studies. Here we propose a novel segmentation framework using an active contour Model to automate area and volume estimation using unbiased stereology. This approach is demonstrated for groups of 3 month-old Fischer 344 rats with experimental Parkinsonism or vehicle-treated controls. Brains were perfused in-vivo with 4% paraformaldehyde and sectioned by frozen microtomy at an instrument setting of 30 um. For each rat brain a total of 12 sections were sampled in a systematic-random manner through the entire substantia nigra (SN). Sampled sections were processed to reveal tyrosine hydroxylase (TH)-immunopositive neurons within the SN. The novel framework applied a balloon active contour model with non-constant balloon force to segment TH-positive neuronal cell bodies followed by size estimation by volume fraction. Several contours were initialized inside the image and based on the contour fit after 200 iterations classified as TH-positive (signal) or background contours in a sequential manner. Cell contours were determined in four steps based on several criteria, e.g., area of contour, dispersion measure, and degree of overlap. The image was automatically segmented according to the final contours. A point grid was automatically placed over the image and points automatically counted within the segmented areas. The final

values from the automatic framework were correlated with findings for ground truth (manual stereology). The results from this study show a strong correlation between data collected by the automatic framework method and ground truth ($R^2 \geq 0.95$). There was a high gain in efficiency (10 fold) for the automatic approach using the proposed model as compared to manual (non-automatic) stereology. These findings give strongly support for future applications of pattern recognition to assess biological objects stained with high signal: noise.

Keywords: stereology, substantia nigra, neuron, segmentation, parkinson, active contour

2010 MSC: 00-01, 99-00

---

1. Introduction

Quantitative analysis of microscopic images using unbiased stereology is a powerful tool for assessing the morphological changes in biological tissues during normal development, aging, and a wide range of diseases. The point counting method provides a simple and straightforward approach to estimate total volume of neurons and nuclei within an anatomically defined region of interest (ROI). A current limitation is that manual data collection using all computerized stereology systems can be costly, time-consuming and prone to subjective human error. The point counting method is carried out on 12 sections sampled in a systematic manner through the ROI and stained to highlight the cells of interest. After the ROI boundary is manually outlined at low power (4x), images are automatically captured at high power (100x objective) across each section. The software overlays a 10 x 10 point grid in a random orientation over each captured image and the user highlights (clicks) the grid points falling on cells of interest. This process repeats for all images and the software computes the total cell volume [1, 2]. Analysis of one case (e.g., ROI in one rat brain) requires between 1-2 hours or more depending on the user's training and quality of the tissue staining.

We have modified the software for a computerized stereology system [Stere-

ologer, Stereology Resource Center, Inc. (SRC), Tampa, FL] to demonstrate a segmentation approach that fully automates the time-consuming data collection step in the point counting method. The approach involves segmentation of high power images followed by feature extraction and determination of points hitting neuronal nuclei. The details of the proposed segmentation method and framework are described in Section 3. The experiments and results are presented in Section 4, and conclusions are in Section 6.

2. Related Work

Data collection automation in the point counting method is rather unexplored. An earlier study used color information from a video signal and RGB threshold values to automatically estimate volume of neuronal nuclei using point counting stereology [3]. That approach, however, was limited to automatic analysis of high signal: noise (S: N) images. In another work [4], authors proposed an adaptive region-based approach to segment neurons and subsequently count the neuron in Neun images. It sets most of the parameters in the algorithm adaptively and therefore, is expected to be invariant to minor to moderate intensity or color changes. One of the major steps in this task, microscopic image segmentation, is a well-studied topic. Image segmentation is the task of finding objects within an image. A range of methods including active contour models [5, 6, 7], watershed segmentation [8, 9] and level sets [10] have been proposed to segment microscopic images for subsequent classification or tracking of biological objects (e.g., cells). In [11], an active contour model and water segmentation are combined in an interesting way to segment different kinds of microscopic images. Since microscopy images must be chemically stained to reveal cells and subcellular components such as nuclei and cytoplasm, deconvolution methods may be used to segment cells based on color information [12]. However, most of these methods are specific to the images they are designed and tested for, and cannot be used in every other microscopy image. Therefore, we propose a model based on balloon snakes [13] as described in following Section.

3. Methodology

Animal tissue for this study was taken from a previous study [14] in an AAV-α-Syn expressing Fischer 344 rat model of Parkinson's disease. Dopaminergic neurons in the rat substantia nigra were immunostained with antibodies to alpha synuclein. Images were captured at high magnification (100x, oil immersion, na 1.3). The goal of the present study was to automatically quantify neuronal nuclei on these images using the active contour model outlined below. The process of automatically segmenting an image and quantifying points falling on cells within the segmented image is as follows. The image is converted to grayscale and 100 active contours, each with 100 control points, are initialized around the grid points of a 10x10 grid. The contours were stopped after 200 iterations. This process will over-detect cell locations and in the following steps we removed some contours and kept the others as final cell contours: A contour is removed if its area is too small or too large. Contours may also be rejected based on their average intensity and intensity dispersion. Non-rejected contours at this point are called cell contours. Since cell contours may overlap, an extra process removes the overlapped contours and keeps the best ones based on their intensity standard error of the mean (SEM). The remaining contours are called final cell contours and image is segmented based on them. The grid points that fall in the segmented area are counted in each image. Fig 1 shows the segmentation process on an image.

3.1. The Proposed Active Contour Model

The generic balloon snake model fails to properly segment cells in the image: with low balloon force, it cannot expand enough inside most of the cells and with high balloon force, it fails to stop expanding at weaker cell boundaries. Therefore, we propose a novel variation of the generic balloon snake as follows.

First, our model does not allow the contour to shrink at any points. This ensures that whether we successfully initialize the contour inside a cell or not, the contour can only expand. Contours allowed to shrink may be attracted to a

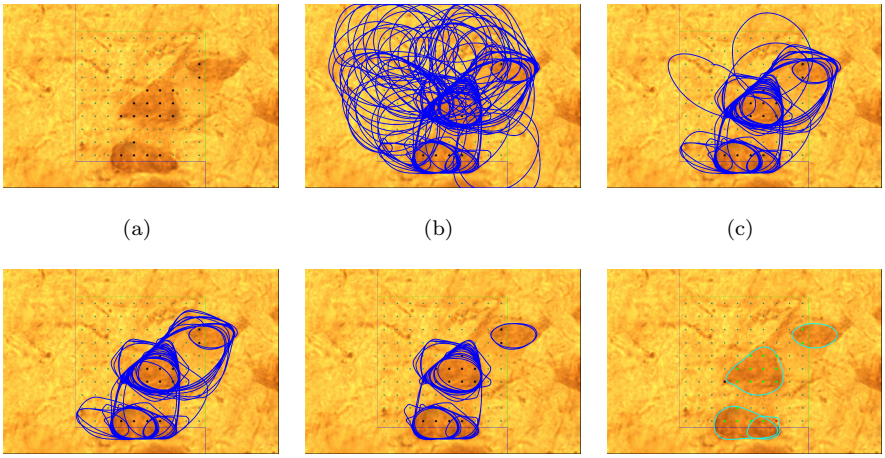

(a) (b) (c)

(d) (e) (f)

Figure 1: (a) The image with manual point marking, (b) all 100 expanded contours, (c) rejecting those which are too large or too small, (d) rejecting those which have average intensity over a threshold, (e) removing those with higher intensity dispersion than a threshold, (f) final result after handling overlapping contours - green marks are true positives, red marks are false positives and black marks are false negatives.

nearby cell with stronger boundary, especially if the original cell has relatively weak boundary. Another benefit is that the contour cannot rotate around small, dark-stained areas such as nuclei. Second, the balloon force changes during the balloon expansion. Starting with a relatively large balloon force we decrease it linearly, as it enlarges more than a threshold, τ_1 (20% of the maximum size in this study). The balloon force stops decreasing after the contour area gets larger than a second threshold, τ_2 (80% of the maximum size). The values of these parameters were chosen empirically on sample images of two cells. The final results are insensitive to small changes in these parameters. Fig. 2 shows the graph of how the balloon force changes as a function of the contour area.

In the following, the automation process based on the proposed model is described in detail.

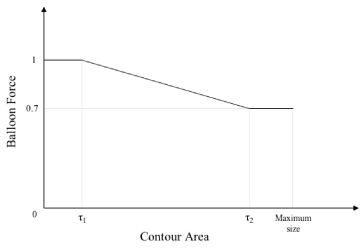

Figure 2: The graph showing how the balloon force changes during the contour expansion.

3.2. Contour Initialization

In the manual process a 10x10 grid is put on the image and the experts choose the cell points by clicking on each grid point. In an automated process, we first put the 10x10 grid on the image and then initialize a contour with 100 points around a circle centered at each of the grid points. The contour iteratively expands to fit to a boundary in 200 iterations.

Up to this point, we over-detect the cells inside the grid. Therefore, in the next part of the process we reject some contours and keep final cell contours to segment the image.

3.3. Contour Rejection

Contours are not necessarily initialized within cell boundaries. That is why when a contour stops expanding, it still may contain some parts of the background. For this reason, after the contour stops expanding, it must be classified as either *cell* contour, which only contains parts of a cell, or as *background* contour, which contains some parts of the background. For each contour we compute μ_c and σ_c which are the average and standard deviation of pixels belonging to the contour area. We then classify a contour as a background contour if it has at least one of the following properties:

a. It has an area smaller than m,

b. It has an area greater than M,

c. Its area average intensity, μ_c, is higher than μ,

d. Its corresponding dispersion measure, $s_c = \mu_c\sigma_c$, is greater than s_f,

where m and M are the thresholds for the minimum and maximum size of the contour not to be classified as a background contour. These two parameters are set based on the image size and are constant for all the images during an experiment. However, μ and s_f are adaptive parameters and are computed separately for each image as follows.

We apply a 2-class Otsu thresholding [15] on the grayscale image. The darker class (with lower average pixel intensity) is marked as foreground (cell) area and the other class will be the background area. The average intensity of the foreground and background classes are denoted by μ_f and μ_b respectively. Then we set

$$\mu = \frac{\mu_b + n\mu_f}{n+1}, \tag{1}$$

where n is a positive integer. The higher values of n give more weight to μ_f than μ_b in computing μ and hence making it close to μ_f. Therefore, the value of n can be tweaked to classify more or less contours as the cell contours.

Let σ_f and σ_b be the standard deviation of foreground and background pixels intensities respectively. Then we define s_f as

$$s_f = \mu_f^2 \left(\frac{\sigma_f}{\mu_f}\right) = \mu_f \sigma_f, \tag{2}$$

which is used as a *measure of dispersion* of the foreground pixels intensity. In computation of s_f, the coefficient variation of pixel intensities in the foreground is multiplied by μ_f^2 to encourage the area which is going to be classified as cell area to be in a darker region as well as having a lower coefficient variation.

After this step, all contours are classified either as cell contour or as background contour. The cell contours usually overlap with each other and therefore, in an extra step we handle overlapping contours.

3.4. Overlapping Contours

The slides used in this study are *thick* slides ($>$ 15 um after all tissue processing). This means that cells appear at different depths (in or out of focus) when the image is acquired. This issue causes the active contours to miss some

of the most shallow and out of focus cells and therefore increases the segmentation error. Because of initial cell over-detection and classifying contours as either cell or background contour, we frequently encounter cell contours that *overlap* with each other. These cell contours are either segmenting the same cell or two different overlapping cells.

To define *overlapping* contours, we set a threshold, θ, and say two contours, c_1 and c_2, are overlapping if

$$\max\left\{\frac{A_c}{A_{c_1}}, \frac{A_c}{A_{c_2}}\right\} > \theta, \tag{3}$$

where θ is the overlapping threshold, A_c is the area of the overlapping surface of contours c_1 and c_2, and finally A_{c_1} and A_{c_2} are the areas of the surfaces covered by contours c_1 and c_2. We then form a graph, G, whose nodes represent the contours, edges represent the overlapping relation. We compute *standard error of the mean* for each node v in G as

$$SEM_c = \frac{\sigma_c}{\sqrt{A_c}}, \tag{4}$$

, where σ_c is the standard deviation of the intensities of pixels inside the contour c represented by v. This measure estimates the uniformness of pixels intensities in the contour area. Iteratively, the contour represented by each node with the minimum standard error of the mean is selected as final cell contour and all nodes adjacent to it are removed from the graph. This process is continued until all nodes are removed. The pseudo code of this algorithm can be found in Algorithm 1.

We use the final cell contours to segment the image and mark the grid points which fall within the segmented area as cell points and count them for each image. The number of cell points from all images make up the number of cell points for each section and subsequently for each rat brain tissue.

4. Experiments and Results

In this section, we present the experiments and results for applying the automatic point counting approach to estimating the total volume of cells im-

Algorithm 1 Handling overlapping contours

while G is not empty **do**

  Select an arbitrary connected component, C, of G

  for each node v, representing contour c, in C **do**

    Compute $SEM_c = \sigma_c / \sqrt{A_c}$

  end for

  Let $c' = \arg\min_c \{SEM_c\}$

  Mark c' as final cell contour

  Remove v and all nodes adjacent to v from G

end while

munostained for tyrosine hydroxylase (TH) in the rat substantia nigra.

4.1. Dataset

The dataset consists of thick sections of four rat brains. Each rat brain consists of 12 sections and tissues are stained with TH using standard immunostaining protocols. Two of the cases (rat brains) are in the control group and the other four have experimental treatment. We denote the cases in control group by A_1 through A_4 and the cases in treated group by B_1 and B_2.

A total of 2563 images at 100x zoom were acquired from all sections of cases and cell points in each image were marked manually. The number of images acquired from each case and the total number of manually marked cell points for each case are summarized in Table 1. The process of acquiring these images and the ground truth are discussed below.

To obtain the ground truth, each section of a rat brain was examined visually under a microscope at 2.5x zoom and analyzed using computer-assisted stereology software (Stereologer). The substantia nigra was outlined manually and under software control a point grid was placed at random across each image. The points which hit the region and are close to cells are selected and for each selected point an image centered at that point, at 100x zoom, is shown. A 10x10 grid is put on each of those images and points which fall within the boundaries

Table 1: Total number of images and manually marked cell points for each case.

	Case	Images	Manually marked cell points
Control Group	A_1	550	3425
	A_2	520	2999
	A_3	405	2311
	A_4	201	1313
Treated Group	B_1	327	2270
	B_2	560	2341

of a cell are selected manually. Each of these images are saved to be processed by the algorithm later. At the end of each process, software summarizes the results for each section and the whole brain. Then the number of marked cell points in each section is reported and also the total cell volume is estimated (based on the provided thickness of each slide).

4.2. Experiments

The proposed algorithm automatically segments the images at 100x zoom, which is then stored during the manual process and the number of grid point which fall within a cell boundary counted.

Most of the parameters, such as $\mu_b, \mu_f, \sigma_b, \sigma_f, \sigma_c, s_f$ are computed adaptively based on each specific image and contours during the process. M is chosen based on image size and τ_1 and τ_2 in (2) are chosen empirically based on three test images. The remaining three parameters, m, n in (1) and θ in (3) are set based on a leave-one-out process, from the possible values below:

$$m \in \{2000, 2500, 3000\},\ n \in \{1, 2, 3\},\ \text{and}\ \theta \in \{65\%, 75\%, 85\%\}.$$

We evaluate the performance based on two measures: Norm of residuals, N_{res} and R^2. Denote the manual count of cell points from 12 sections of a particular

case by x_1 through x_{12} and denote the corresponding automated counts by x_i''s. Norm of residuals is defined as

$$N_{res} = \sqrt{\sum_{i=1}^{12}(x_i - x_i')^2}. \tag{5}$$

Moreover, R^2 for the case is also defined based on x_i's and x_i''s.

4.3. Results

The N_{res}, R^2, automated count and selected set of parameters based on the leave-one-out process is presented in Table 2. At each phase of the leave-one-out processing, the set of parameters which gives the least average norm of residuals on training cases is used for the algorithm to run on the test case.

Table 2: The total count of cell grid points, R^2 and norm of residuals for the testing cases with parameters selected in a leave-one-out process

Case	Man. Count	Auto. Count	R^2	N_{res}	m, n, θ
A_1	3425	3653	0.95	136.48	$2000, 3, 85\%$
A_2	2999	2783	0.98	99.75	$2500, 3, 85\%$
A_3	2311	2429	0.97	103.88	$2500, 3, 85\%$
A_4	1313	1202	0.97	87.82	$3000, 2, 85\%$
B_1	2270	2166	0.97	101.67	$2500, 2, 75\%$
B_2	2341	2254	0.96	103.23	$2500, 3, 85\%$

Fig. 3 shows two more final segmentation and point counting results of sample images.

The code was implemented in Matlab and the average processing time of an image is around 24 seconds on a PC with 3.80 GHz processor and 8 GB of RAM.

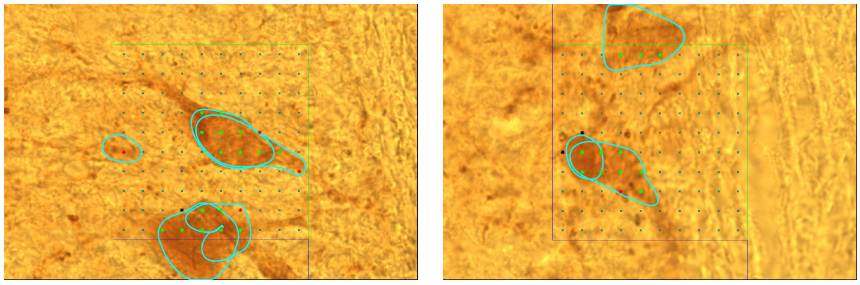

(a) (b)

Figure 3: Two more final results on sample images.

5. Discussion

Although we obtain a cell segmentation inside each image, the ultimate purpose of the proposed framework is to automate the manual process of point counting for stereology studies. The process of point counting is usually used to compare the average cell volume for cases in control group as compared to a treatment group. For validation purposes, the automated method should return a final total count close to that obtained from a manual count. Our results show that although parameters were tuned based on the norm of residuals, the algorithm total count is very close to the manual count. Except for A_3, where the final automated count is barely larger than 105% of the manual count, the differences between automated and manual counts for all other cases is less than 5% of the manual count. Also an R^2 higher than 0.95 shows a high correlation between the manual counts of each section to the corresponded automated count. This difference in the two final manual and automated counts was also present in training cases and can be considered negligible. A number of cells are observed during the manual point counting which had a weak boundaries and/or high staining intensity. The decision of the expert to include each of these cells when encountered can change the final total point count by several percent. As an example, four images including such cells can be seen in Fig. 4. In these images there are cells that are not well enough in focus to be included or excluded decisively.

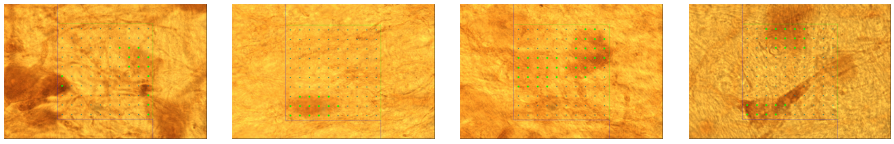

(a) (b) (c) (d)

Figure 4: Samples of images from the case A_2 containing very shallow cells.

Other than those cells, the count inaccuracy in different images may occur because of the segmentation error. The two main sources of errors in segmentation are accuracy of the active contour model and the contour classification process. The contour may not fit to cells or the classification may classify some contours incorrectly. Visual examination showed that the active contour model's accuracy is larger source of errors. The accuracy is affected mostly because of the image quality.

Three main sources of errors are listed below. The first two affect model accuracy and the last causes classification inaccuracy.

1. Images are slightly to moderately out of focus. Slides are obtained from thick sections and therefore cells appear in different depths and focusing on a cell can make other cells to go out of focus. If focus for some cells is poor, real boundaries cannot even be determined by an expert. Therefore, in practice, it is impossible to have an ideal focus and subsequently many cells will appear out of focus and/or with low intensity. False positive error will increase as cells are not segmented. Where possible, thinner slides will avoid this source of error. Cells in acquired images from thin slides will have sharper boundaries and images will have fewer out of focus cells.
2. We smooth the image to weaken noises such as noisy edges. Smoothing less will increase the strength of noisy edges and thus the contour will be attracted to incorrect edges. Smoothing more will make it difficult for the contour to find the edges as they are the main force for overcoming the balloon force and stopping the contour from expanding beyond the

cell boundaries. Therefore the contour may stop at an approximate cell boundary location. This will make the contour unable to segment the whole cell area and therefore some manually marked cell points will not be marked in segmented images. This contributes to false negative errors.

3. The staining process, in this case TH immunostaining, may also stain axons. Based on the strength and thickness of axons in images, they may be segmented as part of the cell body (soma). This can be a difficult source of error to avoid. However, this kind of error is rare because axons are usually less intense and not as thick as cell bodies. In practice, segmented axons may be removed as a source of error using a min blob size check.

Overall, one of the easiest ways to properly increase the quality of images is to use thin slides. Cells in acquired images from thin slides will have sharper boundaries and images will have fewer out of focus cells. This especially helps with more dense and populated images.

6. Conclusions

A framework based on a variation of the balloon snake is proposed to automate the manual process of area and volume estimation of stained biological objects on tissue sections. The framework basically over-detects cells inside each image and then in a selection process reject some contours and keeps the others to segment and detect grid points which fall inside cell boundaries. Contours are initialized around each of the grid points. The main difference between the proposed model and the original balloon snake are the inability of the contour to shrink and the variable balloon force. Three free parameters are set based on a leave-one-out process to run the algorithm on each case. The algorithm segmented a total of 2563 images at 100x zoom from all cases and the results were compared to the ground truth data. The results show a high correlation with the ground truth data and the difference of the final total count of cell points to the manual total count is around 10% of the total manual count. Based on these findings, it can be concluded that the algorithm is providing an

efficient and reliable approach for automating the point counting approach for stereology.

References

[1] P. R. Mouton, Unbiased Stereology: A Concise Guide, The Johns Hopkins University Press, Baltimore, 2011.

[2] P. R. Mouton, Quantitative Anatomy Using Unbiased Stereology, CRC Press, London, 2014.

[3] P. R. Mouton, J. Durgavich, D. K. Ingram, Automatic estimation of size parameters using verified computerized stereoanalysis, Image analysis & stereology 24 (1) (2011) 41–49.

[4] P. R. Mouton, H. Ahmady Phoulady, D. Goldgof, L. O. Hall, M. Gordon, D. Morgan, Unbiased estimation of cell number using the automatic optical fractionator, Journal of chemical neuroanatomy 80 (2017) A1–A8.

[5] H. Zhou, X. Li, G. Schaefer, M. E. Celebi, P. Miller, Mean shift based gradient vector flow for image segmentation, Computer Vision and Image Understanding 117 (9) (2013) 1004 – 1016. doi:http://dx.doi.org/10.1016/j.cviu.2012.11.015.
URL http://www.sciencedirect.com/science/article/pii/S1077314213000751

[6] K. Li, Z. Lu, W. Liu, J. Yin, Cytoplasm and nucleus segmentation in cervical smear images using radiating gvf snake, Pattern Recognition 45 (4) (2012) 1255 – 1264. doi:http://dx.doi.org/10.1016/j.patcog.2011.09.018.
URL http://www.sciencedirect.com/science/article/pii/S0031320311003979

[7] P. Bamford, B. Lovell, Unsupervised cell nucleus segmentation with active contours, Signal Processing 71 (2) (1998) 203 – 213.

doi:http://dx.doi.org/10.1016/S0165-1684(98)00145-5.
URL http://www.sciencedirect.com/science/article/pii/S0165168498001455

[8] X. Yang, H. Li, X. Z., Nuclei segmentation using marker-controlled watershed, tracking using mean-shift, and kalman filter in time-lapse microscopy, Circ. and Sys. I: Regular Papers, IEEE Trans. on 53 (11) (2006) 2405–2414. doi:10.1109/TCSI.2006.884469.

[9] A. Gençtav, S. Aksoy, S. Önder, Unsupervised segmentation and classification of cervical cell images, Pattern Recognition 45 (12) (2012) 4151 – 4168. doi:http://dx.doi.org/10.1016/j.patcog.2012.05.006.
URL http://www.sciencedirect.com/science/article/pii/S0031320312002191

[10] Z. Lu, G. Carneiro, A. P. Bradley, Automated nucleus and cytoplasm segmentation of overlapping cervical cells, in: K. Mori, I. Sakuma, Y. Sato, C. Barillot, N. Navab (Eds.), MICCAI 2013, Vol. 8149 of LNCS, Springer Berlin Heidelberg, 2013, pp. 452–460.

[11] I. Dagher, K. E. Tom, Waterballoons: A hybrid watershed balloon snake segmentation, Image and Vision Computing 26 (7) (2008) 905 – 912. doi:http://dx.doi.org/10.1016/j.imavis.2007.10.010.
URL http://www.sciencedirect.com/science/article/pii/S0262885607001965

[12] M. Veta, P. J. van Diest, R. Kornegoor, A. Huisman, M. A. Viergever, J. P. Pluim, Automatic nuclei segmentation in h&e stained breast cancer histopathology images, PLoS One 8 (7).

[13] C. D. Laurent, On active contour models and balloons, CVGIP: Image Understanding 53 (2) (1991) 211 – 218. doi:http://dx.doi.org/10.1016/1049-9660(91)90028-N.
URL http://www.sciencedirect.com/science/article/pii/104996609190028N

[14] M. Shahaduzzaman, K. Nash, C. Hudson, M. Sharif, B. Grimmig, X. Lin, G. Bai, H. Liu, K. E. Ugen, C. Cao, et al., Anti-human α-synuclein n-terminal peptide antibody protects against dopaminergic cell death and ameliorates behavioral deficits in an aav-α-synuclein rat model of parkinsons disease, PloS one 10 (2) (2015) e0116841.

[15] N. Otsu, A threshold selection method from gray-level histograms, Systems, Man and Cybernetics, IEEE Transactions on 9 (1) (1979) 62–66. doi:10.1109/TSMC.1979.4310076.